

# Mass and energy balance calculations for artificial ice reservoirs (Icestupas)

Suryanarayanan Balasubramanian<sup>1\*</sup>, Martin Hoelzle<sup>1</sup>, Michael Lehning<sup>2</sup>,  
Sonam Wangchuk<sup>3</sup>, Johannes Oerlemans<sup>4</sup>, Felix Keller<sup>5,6</sup> and Jordi Bolíbar<sup>4</sup>

<sup>1</sup> University of Fribourg, Fribourg, Switzerland

<sup>2</sup> WSL Institute for Snow and Avalanche Research, Davos, Switzerland

<sup>3</sup> Himalayan Institute of Alternatives Ladakh, Leh, India

<sup>4</sup> Institute for Marine and Atmospheric Research, Utrecht University, Utrecht, The Netherlands

<sup>5</sup> Academia Engiadina, Samedan, Switzerland

<sup>6</sup> ETH, Zürich, Switzerland

Correspondence\*:

Suryanarayanan Balasubramanian

suryanarayanan.balasubramanian@unifr.ch

## 2 ABSTRACT

Artificial Ice Reservoirs (AIRs) can successfully store water during winter and release the water during spring and summer. This makes them a reliable fresh water resource for irrigation in dry environments. Several AIRs have been built but studies of their water storage capacity and efficiency are scarce. This study models a cone-shaped AIR popularly called Icestupa. Processes involved in the development and temporal evolution of an Icestupa are calculated by a physically-based model using equations governing the heat transfer, vapour diffusion and transport of water that undergoes phase changes. These processes were quantified using meteorological data in conjunction with fountain spray information (mass input of an AIR) to estimate the quantity of frozen, melted, evaporated and runoff water for three sites in Switzerland and one in India. At these measurement sites, AIR were built for model validation purposes. The model was further tested by performing a sensitivity and uncertainty study showing that the most sensitive parameters are the ice emissivity and the temperature threshold used to determine precipitation phase. Model calculations estimate that the AIR stored about % of the total water sprayed as ice.

**Keywords:** iceshelf, mass balance, water storage, climate change adaptation, geoengineering

## 1 INTRODUCTION

Seasonal snow cover, glaciers and permafrost are expected to change their water storage capacity due to climate change with major consequences for downriver water supply (Immerzeel et al., 2019). The challenges brought about by these changes are especially important for dry mountain environments such as in Central Asia or the Andes, which directly rely on the seasonal meltwater for their farming and drinking needs (Hoelzle et al., 2019; Apel et al., 2018; Buytaert et al., 2017; Chen et al., 2016; Unger-Shayesteh et al., 2013). Some villages in Ladakh, India have already been forced to relocate due to glacial retreat and the corresponding loss of their main fresh water resources (Grossman, 2015).



**Figure 1.** Icestupa in Ladakh, India on March 2017 was 24 m tall and contained around 3700 m<sup>3</sup> of water.  
Picture Credits: Lobzang Dadul

24 Artificial ice reservoirs (AIRs) have been considered to be a feasible way to adapt to these changes (Hock  
25 et al., 2019; Nüsser et al., 2019b). An AIR is a human-made ice structure typically constructed during the  
26 cold winter months and designed to slowly release freshwater during the warm and dry spring and summer  
27 months. The main purpose of AIRs is irrigation. Therefore, AIRs are designed to store water in the form of  
28 ice as long into the summer as possible. The energy required to construct an AIR is usually derived from  
29 the gravitational head of the source water body. Some are constructed horizontally by freezing water using  
30 a series of checkdams and others are built vertically by spraying water through fountain systems (Nüsser  
31 et al., 2019a). The latter are colloquially referred to as Icestupas and are the subject of this study.

32 A typical Icestupa just requires a pipeline attached to a vertically mounted metal pipe with a fountain  
33 nozzle for construction. Their water source is usually a high altitude lake or glacial stream. Due to the  
34 altitude difference between the pipeline input and fountain output, water ejects from the fountain nozzle as  
35 droplets that eventually lose their latent heat to the atmosphere and accumulate as ice around the metal pipe.  
36 The fountain nozzle is raised through addition of further pipes as and when significant ice accumulates.  
37 Typically, a dome of branches is constructed around the metal pipe so that such pipe extensions can be  
38 done from within this dome. During the winter, the fountain is manually activated from sunset to sunrise.  
39 Threads, tree branches and fishing nets are used to guide and accelerate the ice formation.

40 Since their invention in 2013 (Wangchuk, 2014), Icestupas have gained widespread publicity in the region  
41 of Ladakh, Northern India since they require very little infrastructure, skills and energy to be constructed  
42 in comparison to other water storage technologies. Compared to other AIR geometries, Icestupas (Fig.  
43 1) can be built at lower altitudes and last much longer into the summer than other types of ice structures  
44 (Wangchuk, 2014). However, to date, no reliable estimates exist about the amount of sprayed water that  
45 is necessary to create them and the meltwater they provide (Nüsser et al., 2019a). Rough estimates of  
46 Icestupa meltwater in Ladakh suggest that the water loss during the construction process is considerable  
47 (see Appendix 7.1). A complete set of measurements of the water storage and energy balance are required  
48 to understand the cause of the water losses better and increase the construction efficiency.

49 In this paper, we aim to develop a physically-based model of a vertical AIR (or Icestupa) that can quantify  
50 their storage efficiency using existing weather and water usage information. Mass and energy balance

**Table 1.** The Scientific AIR

AIR	Gangles, 2021	Guttannen, 2021	Guttannen, 2020	Schwarzsee, 2019
Code	IN21	CH21	CH20	CH19
Altitude [m a.s.l.]	4025	1047	1047	967
Fountain Duration	Jan 18 - Mar 10	Nov 22 - Feb 21	Jan 3 - Feb 27	Jan 30 - Feb 16
Drone Flights	6	9	3	0
$r_{spray}$ [m]	10.8	6.9	7.7	1.2
$V_{dome}$ [m <sup>3</sup> ]	78.5	13.2	23.9	0

51 equations were used to estimate the quantity of water frozen, melted, evaporated and runoff. Sensitivity  
 52 and uncertainty analysis were performed to identify the most critical parameters and the variance caused  
 53 by them. For validation, we chose four AIR built across the winters of 2019, 2020 and 2021 in India and  
 54 Switzerland. Our model and validation experiments provide first steps towards evaluating the effectiveness  
 55 of a vertical AIR for irrigation and allow us to outline some preliminary guidelines for consideration when  
 56 a construction of an Icestupa for water storage is envisaged.

## 2 STUDY SITES

57 To accurately estimate and validate the ice volume of AIR the model requires three kinds of datasets namely,  
 58 weather, water and ice volume. So through the winters of 2019, 2020 and 2021 several scientific AIR were  
 59 constructed by teams in Switzerland and India. Each site had an Automatic Weather Station (AWS) nearby.  
 60 Also drone flights were conducted periodically to record AIR ice volume. For this analysis, we have chosen  
 61 four of the AIR which have a relatively complete dataset associated with them as shown in Table 1.

### 2.1 Construction

62 The construction strategy used in each site varied. CH20 and CH21 AIR was constructed by Guttannen  
 63 Bewegt Association on a garden adjacent to a stream in Guttannen, Switzerland. To initiate the ice formation  
 64 process, tree branches were laid covering the fountain pipe. The fountain height varied between 2 to 5 m  
 65 during the construction period. Fountain operation was guided by temperature conditions.

66 The IN21 AIR was constructed as part of the Icestupa Competition in Gangles, Ladakh, India. It was  
 67 constructed adjacent to another AIR and merged with it. To initiate the ice formation process, a dome of  
 68 2 m radius was constructed and the fountain pipeline was erected at the center using a tripod. Fountain  
 69 operation was interrupted only due to pipeline freezing events. The fountain height varied between 5 to  
 70 9 m.

71 The CH19 AIR was constructed by the Eispalast in Schwarzsee, Switzerland. It was contained inside a  
 72 wooden boundary adjacent to a stream. Fountain operation was guided by temperature conditions. The  
 73 water spray of the fountain was initially adjusted so that most of the water droplets land within the wooden  
 74 boundary zone. The ice formation was guided by adding a metal framework at the ice structure base after  
 75 the first night of operation. Several cotton threads were tied between the ice structure base and fountain  
 76 pole for accelerating and further guiding the ice formation process.

### 2.2 Measurements

#### 2.2.1 Weather measurements

77 Air temperature, relative humidity, wind speed, pressure, longwave, shortwave direct and diffuse radiation  
 78 are required to calculate the surface energy balance of an AIR. All the 4 sites had AWS near the construction

site which measured most of these parameters. The specific corrections applied on the input dataset for each site is described in the Appendix. In addition, we used ERA5 reanalysis dataset (Copernicus Climate Change Service (C3S), 2017) for filling data gaps and adding data that were not measured directly at the respective site. Near-surface humidity is not provided directly in ERA5 dataset, but from near-surface ( $2\text{ m}$  from the surface) temperature ( $T_{ERA5}$ ) and dew point temperature ( $Tw_{ERA5}$ ) the relative humidity ( $RH$ ) at  $2\text{ m}$  was calculated as:

$$RH = 100 \cdot \frac{e_{sat}(Tw_{ERA5})}{e_{sat}(T_{ERA5})} \quad (1)$$

where the saturation vapour pressure function  $e_{sat}$  is expressed with the Teten's formula (Tetens, 1930):

$$e_{sat}(T) = a_1 \cdot e^{(a_3 \cdot \frac{T}{T+273.16-a_4})} \quad (2)$$

with  $T$  in  $^{\circ}\text{C}$  and the parameters set for saturation over water ( $a_1 = 611.21\text{ Pa}$ ,  $a_3 = 17.502$  and  $a_4 = 32.19\text{ K}$ ) according to Buck (1981). Zero wind speed values were recorded whenever snow accumulated on the ultrasonic wind sensor. All such null values were replaced using the ERA5 dataset.

The ERA5 reanalysis dataset has a good correlation with lower elevation sites in Switzerland (Scherrer, 2020) but a poor correlation for the Indian (IN21) site. So the weather dataset for the IN21 site was completed using another AWS nearby as described in the Appendix.

### 2.2.2 Discharge measurements

The water flow rate or discharge was measured via an ultrasonic sensor attached to the fountain supply pipeline for all the sites. However, due to various malfunctions, the discharge measurements were incomplete for all the sites except CH19. Using the hourly webcam images of the CH sites, the discharge duration was determined. The available discharge measurement was later used to determine the average discharge quantity during these periods. For the IN21 site, discharge duration was estimated by manual observations and discharge quantity was arbitrarily set to be  $60\text{ l/min}$ .

### 2.2.3 Ice volume measurements

Several Drone flights were conducted in every AIR site. The DEM generated through these flights were analysed to obtain the circumference and volume of the ice structure. The mean circumference measured during the fountain duration was set as the spray radius ( $r_{spray}$ ) and the first drone flight was used to set the dome volume ( $V_{dome}$ ) for model initialisation. The ice volume data was later used for calibration and validation of the model. There were no drone flights conducted for CH19 AIR, so the  $r_{spray}$  was instead calculated from fountain attributes as described in Appendix.

The model application is restricted to CH21 AIR below. Model results and figures for other AIR can be found in the supplementary materials.

## 2.3 CH21 AIR

The Guttannen (CH21) site in the Bern region lies at  $1047\text{ m a.s.l.}$ . In the winter (Oct-Apr), mean daily minimum and maximum air temperatures vary between  $-13$  and  $15\text{ }^{\circ}\text{C}$ . Clear skies are rare, averaging around 7 days during winter (Meteoblue, 2020). The site was situated adjacent to a stream resulting in high humidity values across the study period as shown in Fig. 9. The fountain used for spraying water had an initial height of  $2.3\text{ m}$ . The water was transferred from a spring water source and flowed via a flowmeter to the nozzle. In addition, a webcam guaranteed a continuous survey of the site during the construction of the AIR.



**Figure 2.** Bird's eye view of the CH21 AIR

119 The weather data was primarily drawn from a meteoswiss AWS located 184 m away from the construction  
120 site. ERA5 dataset was used for filling and adding data as shown in Fig. 3.

### 3 MODEL SETUP

121 A bulk energy and mass balance model is used to calculate the amounts of ice, meltwater, water vapour  
122 and runoff water of the AIR every hour. This model consists of four modules which estimates the AIR, a)  
123 geometric evolution , b) energy balance, c) surface temperature and d) mass balance.

#### 124 3.1 Geometric evolution

125 Radius  $r_{ice}^i$  and height  $h_{ice}^i$  define the dimensions of the AIR assuming its geometry to be a cone. The  
126 surface area  $A^i$  exposed to the atmosphere and volume  $V^i$  are:

$$A = \pi \cdot r_{ice} \cdot \sqrt{r_{ice}^2 + h_{ice}^2} \quad (3)$$

$$V = \pi/3 \cdot r_{ice}^2 \cdot h_{ice} \quad (4)$$

127 Note that we do not specify the time step superscript  $i$  of the shape variables  $A$ ,  $V$ ,  $r_{ice}$  and  $h_{ice}$  for  
128 brevity. The equations used henceforth display model time step superscript  $i$  only if it is different from the  
129 current time step.

130 With the mass of the AIR  $M_{ice}$ , its current volume can also be expressed as:

$$V = M_{ice}/\rho_{ice} \quad (5)$$

131 where  $\rho_{ice}$  is the density of ice ( $917 \text{ kg m}^{-3}$ ).

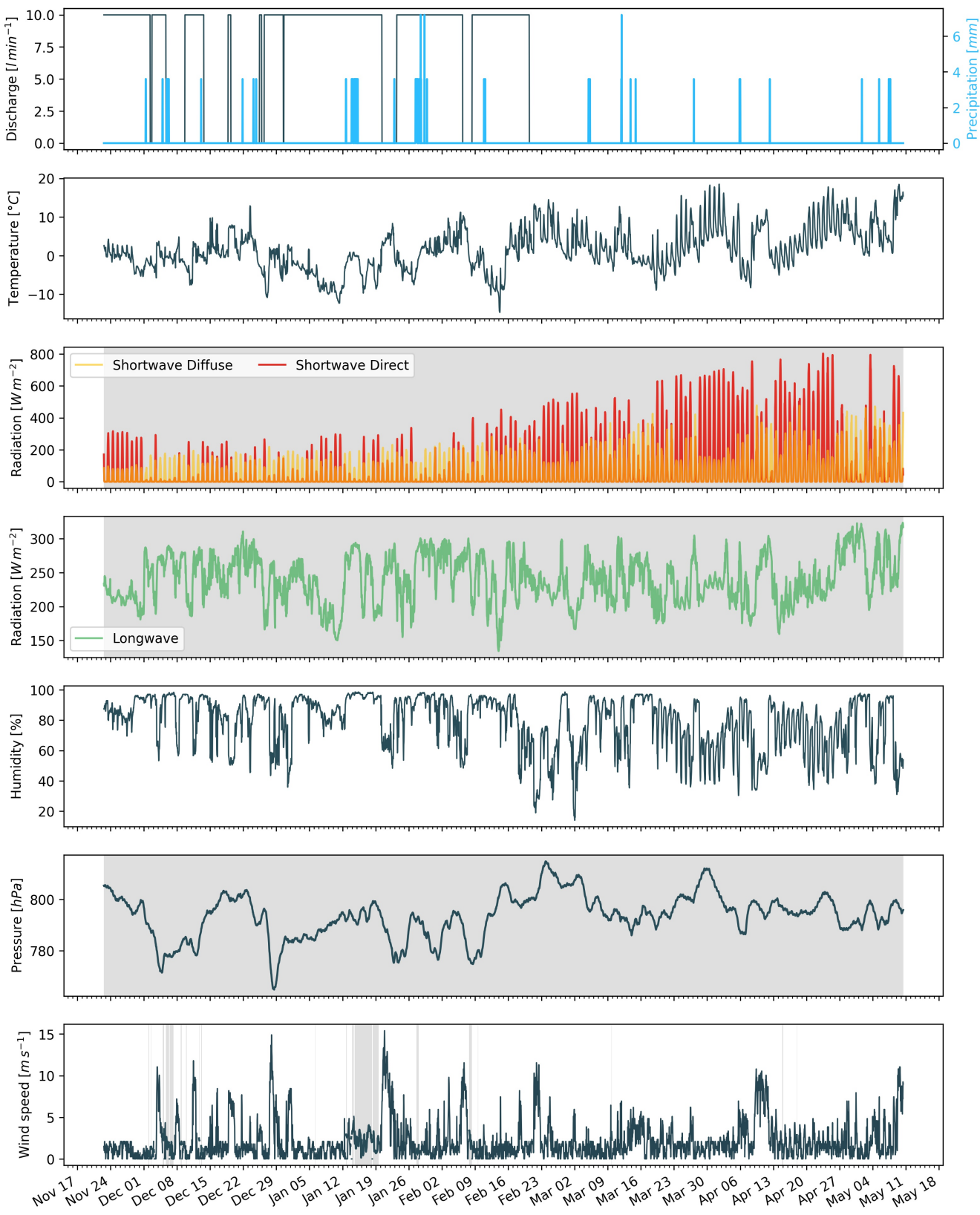


**Figure 3.** Measurements at the AWS of CH21 were used as main model input data in hourly frequency. Missing data, data gaps and errors were filled from the ERA5 dataset (shaded regions).

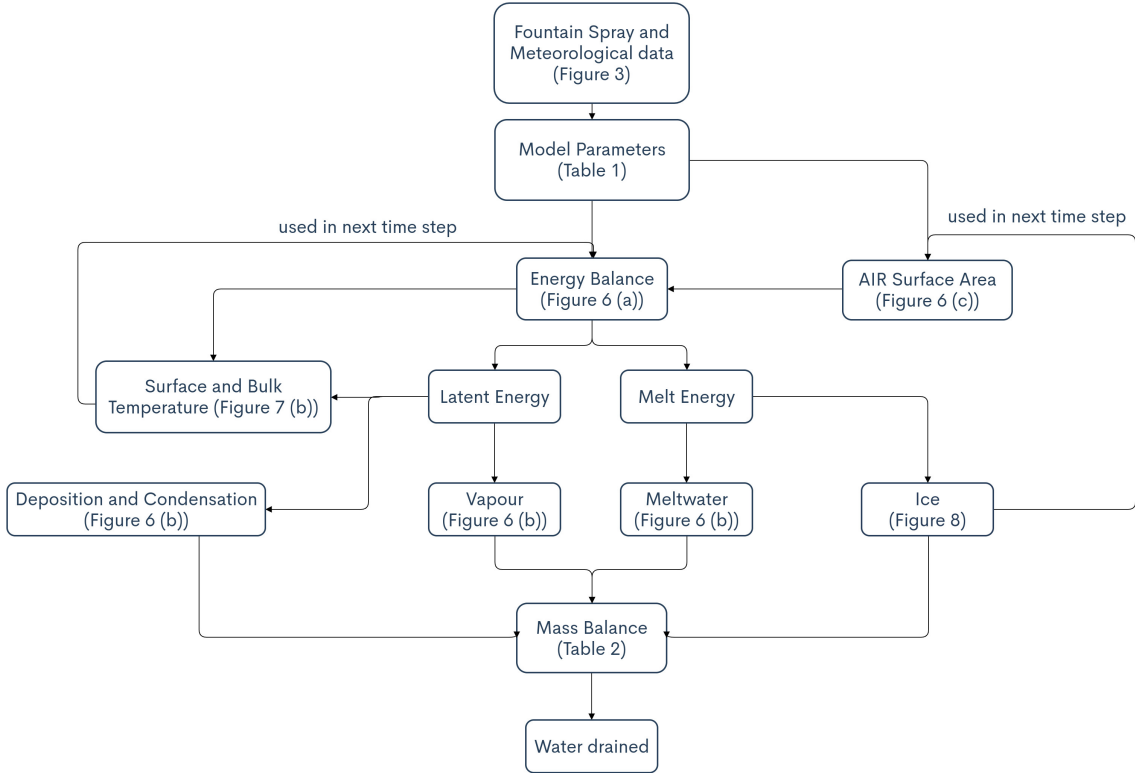


**Figure 4.** Model schematic showing the algorithm used in the model at every time step. Further details about the variables can be found in the associated tables and figures.

132 The influence of the AIR fountain is parameterised by the fountain water temperature  $T_w$  and its spray  
 133 radius  $r_{spray}$ . The initial radius  $r_0$  of the AIR is assumed to be  $r_{spray}$ . The initial height  $h_0$  depends on the  
 134 dome volume  $V_{dome}$  used to construct the AIR as follows:

$$h_0 = \Delta x + \frac{3 \cdot V_{dome}}{\pi r_{spray}^2} \quad (6)$$

135 where  $\Delta x$  is the surface layer thickness (defined in Section 3.2)

136 During subsequent time steps, the dimensions of the AIR evolve assuming a uniform ice formation and  
 137 decay across its surface area with an invariant slope  $s_{cone} = \frac{h_{ice}}{r_{ice}}$ . During these time steps, the volume is  
 138 parameterised using Eqn. 4 as:

$$V = \frac{\pi \cdot r_{ice}^3 \cdot s_{cone}}{3} \quad (7)$$

139 However, the Icestupa cannot outgrow the maximum range of the water droplets ( $(r_{ice})_{max} = r_F$ ).  
 140 Combining equations 4, 6, 5 and 7, the geometric evolution of the Icestupa at each time step  $i$  can be  
 141 determined by considering the following rules:

$$(r_{ice}, h_{ice}) = \begin{cases} (r_{spray}, h_0) & \text{if } i = 0 \\ (r_{ice}^{i-1}, \frac{3 \cdot M_{ice}}{\pi \cdot \rho_{ice} \cdot (r_{ice}^{i-1})^2}) & \text{if } r_{ice}^{i-1} \geq r_F \text{ and } \Delta M_{ice} > 0 \\ (\frac{3 \cdot M_{ice}}{\pi \cdot \rho_{ice} \cdot s_{cone}})^{1/3} \cdot (1, s_{cone}) & \text{otherwise} \end{cases} \quad (8)$$

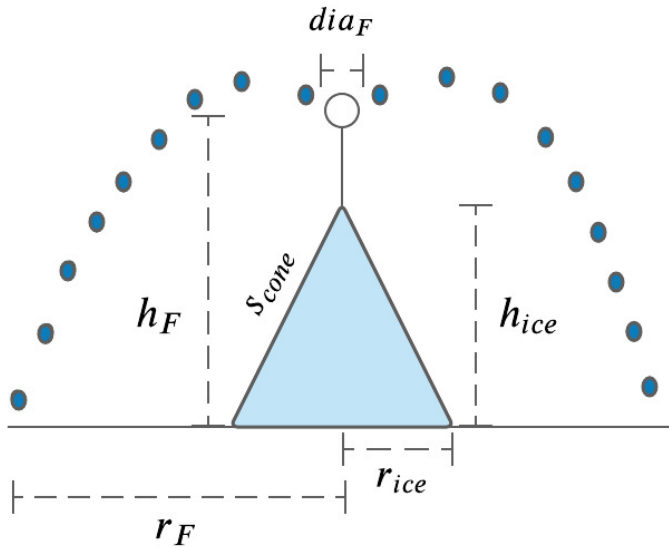


**Figure 5.** Shape variables and fountain constants of the CH21 Icestupa.  $r_{ice}$  is the radius,  $h_{ice}$  is the height and  $s_{cone}$  is the slope of the ice cone.  $r_{spray}$  is the spray radius,  $h_F$  is the height and  $dia_F$  is the nozzle diameter of the fountain.

142 where  $\Delta M_{ice} = M_{ice}^{i-1} - M_{ice}^{i-2}$   
 143 **3.2 Energy Balance**

144 The energy balance equation (Hock, 2005) for the AIR is formulated as follows:

$$q_{SW} + q_{LW} + q_L + q_S + q_F + q_G = q_{surf} \quad (9)$$

145 where  $q_{surf}$  is the surface energy flux in  $[W\ m^{-2}]$ ;  $q_{SW}$  is the net shortwave radiation;  $q_{LW}$  is the net  
 146 longwave radiation;  $q_L$  and  $q_S$  are the turbulent latent and sensible heat fluxes.  $q_F$  represents the heat  
 147 exchange of the fountain water droplets with the AIR ice surface.  $q_G$  represents ground heat flux between  
 148 Icestupa surface and Icestupa interior. Energy transferred in the direction of the ice surface is always  
 149 denoted as positive and away as negative.

150 Equation 9 is usually referred to as the energy budget for “the surface”, but practically it must apply  
 151 to a surface layer of ice with a finite thickness  $\Delta x$ . The energy flux acts upon the Icestupa surface layer  
 152 which has an upper and a lower boundary defined by the atmosphere and the ice body of the Icestupa,  
 153 respectively. The parameter selection for  $\Delta x$  is based on the following two arguments: (a) the ice thickness  
 154  $\Delta x$  should be small enough to represent the surface temperature variations every model time step  $\Delta t$  and  
 155 (b)  $\Delta x$  should be large enough for these temperature variations to not reach the bottom of the surface layer.  
 156 Therefore, we introduced a 20 mm thick surface layer for a model time step of 1 hour, over which the  
 157 energy balance is calculated. A sensitivity analysis was later performed to understand the influence of this  
 158 factor. Here, we define the surface temperature  $T_{ice}$  to be the modelled average temperature of the Icestupa  
 159 surface layer and the energy flux  $q_{surf}$  is assumed to act uniformly across the Icestupa area  $A$ .

160 3.2.1 Net Shortwave Radiation  $q_{SW}$ 161 The net shortwave radiation  $q_{SW}$  is computed as follows:

$$q_{SW} = (1 - \alpha) \cdot (SW_{direct} \cdot f_{cone} + SW_{diffuse}) \quad (10)$$

162 where  $SW_{direct}$  and  $SW_{diffuse}$  are the ERA5 direct and diffuse short wave radiation,  $\alpha$  is the modelled  
163 albedo and  $f_{cone}$  is the area fraction of the ice structure exposed to the direct shortwave radiation.164 We model the albedo using a scheme described in Oerlemans and Knap (1998). The scheme records the  
165 decay of albedo with time after fresh snow is deposited on the surface.  $\delta t$  records the number of time steps  
166 after the last snowfall event. After snowfall, albedo changes over a time step,  $\delta t$ , as

$$\alpha = \alpha_{ice} + (\alpha_{snow} - \alpha_{ice}) \cdot e^{(-\delta t)/\tau} \quad (11)$$

167 where  $\alpha_{ice}$  is the bare ice albedo value (0.35),  $\alpha_{snow}$  is the snow ice albedo value (0.85) and  $\tau$  is a decay  
168 rate, which determines how fast the albedo of the ageing snow reaches this value. The decay rate  $\tau$  is  
169 assumed to have a base value of 10 days similar to values obtained by Schmidt et al. (2017) for wet surfaces  
170 and its maximal value is set based on observations by Oerlemans and Knap (1998) as shown in Table 2.  
171 Furthermore, the albedo  $\alpha$  varies depending on the water source that formed the current Icestupa surface.  
172 Correspondingly, the albedo is reset to the value of bare ice albedo if the fountain is spraying water onto  
173 the current ice surface and to the value of fresh snow albedo if a snowfall event occurred. Snowfall events  
174 are assumed if the air temperature is below  $T_{ppt} = 1^{\circ}C$  (Fujita and Ageta, 2000).175 The area fraction  $f_{cone}$  of the ice structure exposed to the direct shortwave radiation depends on the  
176 shape considered. The direct solar radiation incident on the AIR surface is first decomposed into horizontal  
177 and vertical components using the solar elevation angle  $\theta_{sun}$ . For a conical shape, half of the total curved  
178 surface is exposed to the vertical component of the direct shortwave radiation and the projected triangle  
179 of the curved surface is exposed to the horizontal component of the direct shortwave radiation. The solar  
180 elevation angle  $\theta_{sun}$  used is modelled using the parametrisation proposed by Woolf (1968). Accordingly,  
181  $f_{cone}$  is determined as follows:

$$f_{cone} = \frac{(0.5 \cdot r_{ice} \cdot h_{ice}) \cdot \cos\theta_{sun} + (\pi \cdot r_{ice}^2 / 2) \cdot \sin\theta_{sun}}{\pi \cdot r_{ice} \cdot (r_{ice}^2 + h_{ice}^2)^{1/2}} \quad (12)$$

182 The ERA5 diffuse shortwave radiation is assumed to impact the conical Icestupa surface uniformly.

183 3.2.2 Net Longwave Radiation  $q_{LW}$ 184 The net longwave radiation  $q_{LW}$  is determined as follows:

$$q_{LW} = LW_{in} - \sigma \cdot \epsilon_{ice} \cdot (T_{ice} + 273.15)^4 \quad (13)$$

185 where  $T_a$  represents the measured air temperature,  $T_{ice}$  is the modelled surface temperature, both  
186 temperatures are given in  $^{\circ}C$ ,  $\sigma = 5.67 \cdot 10^{-8} J m^{-2} s^{-1} K^{-4}$  is the Stefan-Boltzmann constant,  $LW_{in}$   
187 denotes the incoming longwave radiation derived from the ERA5 dataset and  $\epsilon_{ice}$  is the corresponding  
188 emissivity value for the Icestupa surface (see Table 2).

189 3.2.3 Turbulent sensible  $q_S$  and latent  $q_L$  heat fluxes

190 The turbulent sensible  $q_S$  and latent heat  $q_L$  fluxes are computed with the following expressions proposed  
 191 by Garratt (1992):

$$q_S = c_a \cdot \rho_a \cdot p_a / p_{0,a} \cdot \frac{\kappa^2 \cdot v_a \cdot (T_a - T_{ice})}{(\ln \frac{h_{AWS}}{z_{ice}})^2} \quad (14)$$

$$q_L = 0.623 \cdot L_s \cdot \rho_a / p_{0,a} \cdot \frac{\kappa^2 \cdot v_a (p_{v,a} - p_{v,ice})}{(\ln \frac{h_{AWS}}{z_{ice}})^2} \quad (15)$$

192 where  $h_{AWS}$  is the measurement height above the ground surface of the AWS (in m),  $v_a$  is the wind  
 193 speed in [ $m s^{-1}$ ],  $c_a$  is the specific heat of air at constant pressure ( $1010 J kg^{-1} K^{-1}$ ),  $\rho_a$  is the air density  
 194 at standard sea level ( $1.29 kg m^{-3}$ ),  $p_{0,a}$  is the air pressure at standard sea level ( $1013 hPa$ ),  $\kappa$  is the  
 195 von Karman constant (0.4),  $L_s$  is the heat of sublimation ( $2848 kJ kg^{-1}$ ) and  $z_{ice}$  (1.7 mm) denotes the  
 196 roughness length of ice (momentum and scalar). The vapor pressures over air ( $p_{v,a}$ ) and ice ( $p_{v,ice}$ ) was  
 197 obtained using the following formulation given in WMO (2018):

$$\begin{aligned} p_{v,a} &= 6.107 \cdot 10^{(7.5 \cdot T_a / (T_a + 237.3))} \\ p_{v,ice} &= (1.0016 + 3.15 \cdot 10^{-6} \cdot p_a - 0.074 \cdot p_a^{-1}) \cdot (6.112 \cdot e^{(22.46 \cdot T_{ice} / (T_{ice} + 272.62)))}) \end{aligned} \quad (16)$$

198 where  $p_a$  is the measured air pressure in [hPa].

199 3.2.4 Fountain water heat flux  $q_F$

200 The interaction between the fountain water and the ice surface is taken into account by assuming that  
 201 the ice surface temperature remains constant at  $0^\circ C$  during time steps when the fountain is active. This  
 202 process can be divided into two simultaneous steps: (a) the water temperature  $T_{water}$  is cooled to  $0^\circ C$   
 203 and (b) the ice surface temperature is warmed to  $0^\circ C$ . Process (a) transfers the necessary energy for  
 204 process (b) throughout the fountain runtime. We further assume that this process is instantaneous, i.e. the  
 205 ice temperature is immediately set to  $0^\circ C$  within just one time step  $\Delta t$  when the fountain is switched on.  
 206 Thus, the heat flux caused by the fountain water is calculated as follows:

$$q_F = \begin{cases} 0 & \text{if } \Delta M_F = 0 \\ \frac{\Delta M_F \cdot c_{water} \cdot T_{water}}{\Delta t \cdot A} + \frac{\rho_{ice} \cdot \Delta x \cdot c_{ice} \cdot T_{ice}}{\Delta t} & \text{if } \Delta M_F > 0 \end{cases} \quad (17)$$

207 with  $c_{ice}$  as the specific heat of ice.

208 3.2.5 Bulk Icestupa heat flux  $q_G$

209 The bulk Icestupa heat flux  $q_G$  corresponds to the ground heat flux in normal soils and is caused by the  
 210 temperature gradient between the surface layer ( $T_{ice}$ ) and the ice body ( $T_{bulk}$ ). It is expressed by using the  
 211 heat conduction equation as follows:

$$q_G = k_{ice} \cdot (T_{bulk} - T_{ice}) / l_{ice} \quad (18)$$

**Table 2.** Free parameters in the model categorised as constant, uncertain and site parameters. Base value (B) and uncertainty (U) were taken from the literature. For assumptions (assum.), the uncertainty was chosen to be relatively large (5 %). For measurements (meas.), the uncertainty due to parallax errors is chosen to be (1 %).

Constant Parameters	Symbol	Value	References
Van Karman constant	$\kappa$	0.4	B: Cuffey and Paterson
Stefan Boltzmann constant	$\sigma$	$5.67 \cdot 10^{-8} W m^{-2} K^{-4}$	B: Cuffey and Paterson
Air pressure at sea level	$p_{0,a}$	1013 hPa	B: Mölg and Hardy
Density of water	$\rho_w$	$1000 kg m^{-3}$	B: Cuffey and Paterson
Density of ice	$\rho_{ice}$	$917 kg m^{-3}$	B: Cuffey and Paterson
Density of air	$\rho_a$	$1.29 kg m^{-3}$	B: Mölg and Hardy
Specific heat of ice	$c_{ice}$	$2097 J kg^{-1} ^\circ C^{-1}$	B: Cuffey and Paterson
Specific heat of water	$c_w$	$4186 J kg^{-1} ^\circ C^{-1}$	B: Cuffey and Paterson
Specific heat of air	$c_a$	$1010 J kg^{-1} ^\circ C^{-1}$	B: Mölg and Hardy
Thermal conductivity of ice	$k_{ice}$	$2.123 W m^{-1} K^{-1}$	B: Bonales et al.
Latent Heat of Sublimation	$L_s$	$2848 kJ kg^{-1}$	B: Cuffey and Paterson
Latent Heat of Fusion	$L_f$	$334 kJ kg^{-1}$	B: Cuffey and Paterson
Uncertain Parameters		Range	
Precipitation	$T_{ppt}$	$1 ^\circ C$	$\pm 1 ^\circ C$
Temperature threshold			B + U: Fujita and Ageta, Zhou et al.
Ice Emissivity	$\epsilon_{ice}$	0.95	[0.949,0.993]
Ice Albedo	$\alpha_{ice}$	0.35	$\pm 5 \%$
Snow Albedo	$\alpha_{snow}$	0.85	$\pm 5 \%$
Albedo Decay Rate	$\tau$	10 days	[1, 22] days
Surface layer thickness	$\Delta x$	20 mm	[1, 10] mm
Fountain Parameters		Range	
Spray Radius	$r_{spray}$		$\pm 5 \%$
Water temperature	$T_{water}$	$1 ^\circ C$	[0, 5] $^\circ C$

212 where  $k_{ice}$  is the thermal conductivity of ice ( $2.123 W m^{-1} K^{-1}$ ),  $T_{bulk}$  is the mean temperature of the  
 213 ice body within the Icestupa and  $l_{ice}$  is the average distance of any point in the surface to any other point in  
 214 the ice body.  $T_{bulk}$  is initialised as  $0 ^\circ C$  and later determined from Eqn. 18 as follows:

$$T_{bulk}^{i+1} = T_{bulk} - (q_G \cdot A \cdot \Delta t) / (M_{ice} \cdot c_{ice}) \quad (19)$$

215 Since AIR's typically have conical shapes with  $r_{ice} >> h_{ice}$ , we assume that the center of mass of the ice  
 216 body is near the base of the fountain. Thus, the distance of every point in the AIR surface layer from the ice  
 217 body's center of mass is between  $h_{ice}$  and  $r_{ice}$ . So we calculate  $q_G$  here assuming  $l_{ice} = (r_{ice} + h_{ice})/2$ .

218 **3.3 Surface temperature**

219 The available energy  $q_{surf}$  can act on the surface of the AIR to a) change its temperature, b) melt ice or  
220 c) freeze ice. So Eqn. 9 can be rewritten as:

$$q_{surf} = q_{freeze/melt} + q_T \quad (20)$$

221 where  $q_T$ ,  $q_{freeze}$  and  $q_{melt}$  represent energy associated with process (a), (b) and (c) respectively.

222 To distribute the surface energy flux into these three components, we categorize the model time steps  
223 as freezing or melting events. Freezing events can only occur if there is fountain water available and the  
224 surface energy flux is negative. But just these two conditions are not sufficient as the latent heat energy  
225 can only contribute to temperature fluctuations. So to prevent latent heat energy from turning a melting  
226 event into a freezing event an additional condition namely  $(q_{surf} - q_L) < 0$  is required. Thus, freezing and  
227 melting events are identified as follows:

$$q_{freeze/melt} = \begin{cases} q_{freeze} & \text{if } \Delta M_F > 0 \text{ and } q_{surf} < 0 \text{ and } (q_{surf} - q_L) < 0 \\ q_{melt} & \text{otherwise} \end{cases} \quad (21)$$

228 During a freezing event, the available energy  $(q_{surf} - q_L)$  can either be sufficient or insufficient to  
229 freeze the fountain water available. If insufficient, the additional energy further cools down the surface  
230 temperature. So the surface energy flux distribution during a freezing event can be represented as:

$$(q_{freeze}, q_T) = \begin{cases} (q_{surf} - q_L, q_L) & \text{if } \Delta M_F \geq -\frac{(q_{surf} - q_L)A \cdot \Delta t}{L_f} \\ \left(\frac{\Delta M_F \cdot L_f}{A \cdot \Delta t}, q_{surf} + \frac{\Delta M_F \cdot L_f}{A \cdot \Delta t}\right) & \text{if } \Delta M_F < -\frac{(q_{surf} - q_L)A \cdot \Delta t}{L_f} \end{cases} \quad (22)$$

231 During a melting event, the surface energy flux ( $q_{surf}$ ) is first used to change the surface temperature to  
232  $T_{temp}$  calculated as:

$$T_{temp} = \frac{q_{surf} \cdot \Delta t}{\rho_{ice} \cdot c_{ice} \cdot \Delta x} + T_{ice} \quad (23)$$

233 If  $T_{temp} > 0^\circ C$ , then energy is reallocated from  $q_T$  to  $q_{melt}$  to maintain surface temperature at melting  
234 point. So the surface energy flux distribution during a melting event can be represented as:

$$(q_{melt}, q_T) = \begin{cases} (0, q_{surf}) & \text{if } T_{temp} < 0 \\ \left(\frac{T_{temp} \cdot \rho_{ice} \cdot c_{ice} \cdot \Delta x}{\Delta t}, q_{surf} - \frac{T_{temp} \cdot \rho_{ice} \cdot c_{ice} \cdot \Delta x}{\Delta t}\right) & \text{if } T_{temp} > 0 \end{cases} \quad (24)$$

235 **3.4 Mass Balance**

236 The mass balance equation for an AIR is represented as:

$$\frac{\Delta M_F + \Delta M_{ppt} + \Delta M_{dep}}{\Delta t} = \frac{\Delta M_{ice} + \Delta M_{water} + \Delta M_{sub} + \Delta M_{runoff}}{\Delta t} \quad (25)$$

237 where  $M_F$  is the discharge of the fountain;  $M_{ppt}$  is the cumulative precipitation;  $M_{dep}$  is the cumulative  
238 accumulation through water vapour deposition;  $M_{ice}$  is the cumulative mass of ice;  $M_{water}$  is the cumulative  
239 mass of melt water;  $M_{sub}$  represents the cumulative water vapor loss by sublimation and  $M_{runoff}$  represents

240 the fountain discharge runoff that did not interact with the AIR. The LHS of equation 25 represents the rate  
241 of mass input and the RHS represents the rate of mass output for an AIR.

242 Precipitation input is calculated as shown in equation 26a where  $\rho_w$  is the density of water (1000  
243  $kg\ m^{-3}$ ),  $ppt$  is the measured precipitation rate in [ $m\ s^{-1}$ ] and  $T_{ppt}$  is the temperature threshold below  
244 which precipitation falls as snow. Here, snowfall events were identified using  $T_{ppt}$  as  $1^{\circ}C$ . Snow mass  
245 input is calculated by assuming a uniform deposition over the entire circular footprint of the Icestupa.

246 The latent heat flux is used to estimate either the evaporation and condensation processes or sublimation  
247 and deposition processes as shown in equation 26b. During time steps at which surface temperature is  
248 below  $0^{\circ}C$  only sublimation and deposition can occur, but if the surface temperature reaches  $0^{\circ}C$ ,  
249 evaporation and condensation can also occur. As the differentiation between evaporation and sublimation  
250 (and condensation and deposition) when the air temperature reaches  $0^{\circ}C$  is challenging, we assume  
251 that negative (positive) latent heat fluxes correspond only to sublimation (deposition), i.e. no evaporation  
252 (condensation) is calculated.

253 Since we have categorized every time step as a freezing and melting event, we can determine the meltwater  
254 and ice generated using the associated energy fluxes as shown in equations 26c and 26d. Having calculated  
255 all the other mass components the fountain wastewater generated every time step can be calculated using  
256 equation 26e.

$$\frac{\Delta M_{ppt}}{\Delta t} = \begin{cases} \pi \cdot r_{ice}^2 \cdot \rho_w \cdot ppt & \text{if } T_a < T_{ppt} \\ 0 & \text{if } T_a \geq T_{ppt} \end{cases} \quad (26a)$$

$$\left( \frac{\Delta M_{dep}}{\Delta t}, \frac{\Delta M_{sub}}{\Delta t} \right) = \begin{cases} \frac{q_L \cdot A}{L_s} \cdot (1, 0) & \text{if } q_L \geq 0 \\ \frac{q_L \cdot A}{L_s} \cdot (0, -1) & \text{if } q_L < 0 \end{cases} \quad (26b)$$

$$\frac{\Delta M_{water}}{\Delta t} = \frac{q_{melt} \cdot A}{L_f} \quad (26c)$$

$$\frac{\Delta M_{ice}}{\Delta t} = \frac{q_{freeze} \cdot A}{L_f} + \frac{\Delta M_{ppt}}{\Delta t} + \frac{\Delta M_{dep}}{\Delta t} - \frac{\Delta M_{sub}}{\Delta t} - \frac{\Delta M_{melt}}{\Delta t} \quad (26d)$$

$$\frac{\Delta M_{runoff}}{\Delta t} = \frac{\Delta M_F - \Delta M_{ice}}{\Delta t} \quad (26e)$$

257 To estimate the mass of any component at time step  $i$ , one can now sum the mass flux estimated above:

$$M_{comp}^i = \sum_{t=0}^{t=i} \left( \frac{\Delta M_{comp}}{\Delta t} \right)_t + M_{comp}^0 \quad (27)$$

258 where

$$M_{comp}^0 = \begin{cases} -V_{dome} * \rho_{ice} & \text{if } M_{comp} = M_{ice} \text{ or } M_F \\ 0 & \text{otherwise} \end{cases} \quad (28)$$

259 Considering AIRs as water reservoirs, we can quantify their potential through the amount of water they  
 260 store (storage quantity) and the length of time they store it (storage duration). Another means of comparing  
 261 different Icestupas is through their water storage efficiency defined accordingly as:

$$\text{Storage Efficiency} = \frac{M_{\text{water}}}{(M_F + M_{\text{ppt}} + M_{\text{dep}})} \cdot 100 \quad (29)$$

## 4 MODEL RESULTS

262 The model was forced with meteorological data from 22<sup>nd</sup> November to 10<sup>th</sup> May 2021 (Fig. 3) and  
 263 various parameters (see Table 2) to calculate the mass and energy balance of the CH21 AIR.

### 4.1 Energy and mass balance calculation

265 Daily averages of some components of the energy balance are shown in Fig. 6 (b). On average during  
 266 the experiment duration, the total energy balance was almost zero. Net shortwave radiation ( $35 \text{ W m}^{-2}$ ),  
 267 sensible ( $41 \text{ W m}^{-2}$ ) and latent heat flux ( $2 \text{ W m}^{-2}$ ) with a mostly positive flux towards the surface of the  
 268 icestupa were compensated by the net longwave radiation (-  $47 \text{ W m}^{-2}$ ), the fountain water heat flux (-  
 269  $13 \text{ W m}^{-2}$ ) and the freeze/melt energy (-  $19 \text{ W m}^{-2}$ ). The contributions of other fluxes were negligible in  
 270 comparison.

271 Net shortwave radiation is the main input to, and the most varying energy flux on the ice surface. Its  
 272 variability is controlled by the surface albedo  $\alpha$  and the area fraction  $f_{\text{cone}}$  which therefore represent key  
 273 variables in the energy balance (Fig. 7 (b)). Although global radiation flux reached a daily maximum value  
 274 of  $340 \text{ W m}^{-2}$ ,  $q_{\text{SW}}$  only went up to  $114 \text{ W m}^{-2}$ . This is caused by the fact that less than 40 % of the direct  
 275 solar radiation influenced the Icestupa surface as shown by the area fraction  $f_{\text{cone}}$  in Fig. 7 (a). Snowfall is  
 276 the atmospheric variable connected most closely and proportionally to albedo. Higher and/or more frequent  
 277 snowfall thus decreases the energy available for melt due to the corresponding increase in  $\alpha$ .

278  $q_{\text{LW}}$  was predominantly negative indicating that this energy balance component drove the freezing of  
 279 the ice structure. Daily values of  $q_{\text{LW}}$  ranged from -101 to  $19 \text{ W m}^{-2}$ . Turbulent sensible heat flux  $q_S$   
 280 contributed mostly to the melt of the ice structure. Daily values of  $q_S$  ranged from -3 to  $410 \text{ W m}^{-2}$ . Daily  
 281 values of the turbulent latent heat flux  $q_L$  ranged from -90 to  $157 \text{ W m}^{-2}$ . Since the mean of  $q_L$  was positive,  
 282 the Icestupa gained mass cumulatively from the atmosphere due to the deposition process. Daily values  
 283 of fountain water heat flux ranged from -119 to  $4 \text{ W m}^{-2}$ .  $q_F$  was also a significant contributor to the  
 284 freezing process like  $q_{\text{LW}}$ . So the influence of the fountain on the energy balance and the freezing events  
 285 was significant. The contribution of heat flux by conduction  $q_G$  was minimal as it only varied between  
 286 -1 to  $3 \text{ W m}^{-2}$  with a mean of  $0 \text{ W m}^{-2}$ . The energy contributing to surface temperature changes ( $q_T$ )  
 287 was insignificant in comparison to the energy spent on freezing and melting ( $q_{\text{freeze/melt}}$ ). The resulting  
 288 bulk temperature and the surface temperature are shown in Fig. 7 (b). For the total considered period,  
 289  $q_{\text{freeze/melt}}$  accounted for 30% of overall energy turnover. The energy turnover is calculated as the sum of  
 290 energy fluxes in absolute values.  $q_{\text{LW}}$  accounted for 22%, followed by  $q_S$  (20%),  $q_{\text{SW}}$  (16%),  $q_L$  (5%),  $q_F$   
 291 (6%),  $q_T$  (1%) and  $q_G$  (0%).

292 Fig. 6 (c) represents the mass fluxes associated with these energy exchanges expressed in  $m$  w.e. It shows  
 293 the ice and meltwater formed due to  $q_{\text{melt}}$ , snow accumulated due to precipitation, water vapour deposition  
 294 and sublimation due to  $q_L$ .

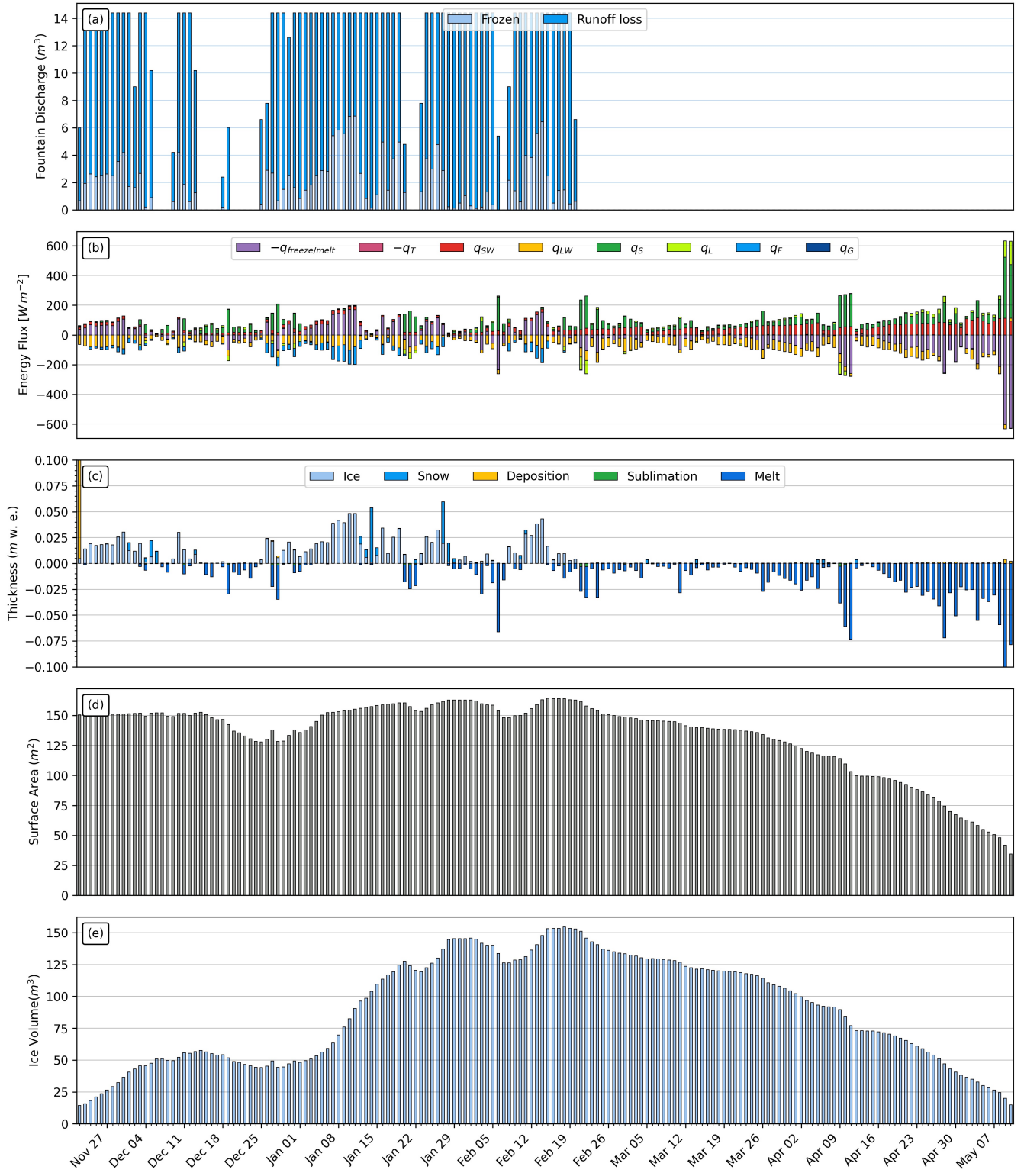


**Figure 6.** (a) Fountain discharge (b) energy flux components, (c) mass flux components (d) surface area and (e) volume of the Icestupa in daily time steps.  $q_{SW}$  is the net shortwave radiation;  $q_{LW}$  is the net longwave radiation;  $q_L$  and  $q_S$  are the turbulent latent and sensible heat fluxes.  $q_F$  represents the interactions of the fountain water with the AIR surface layer.  $q_G$  quantifies the heat conduction process between the AIR surface layer and the ice body.

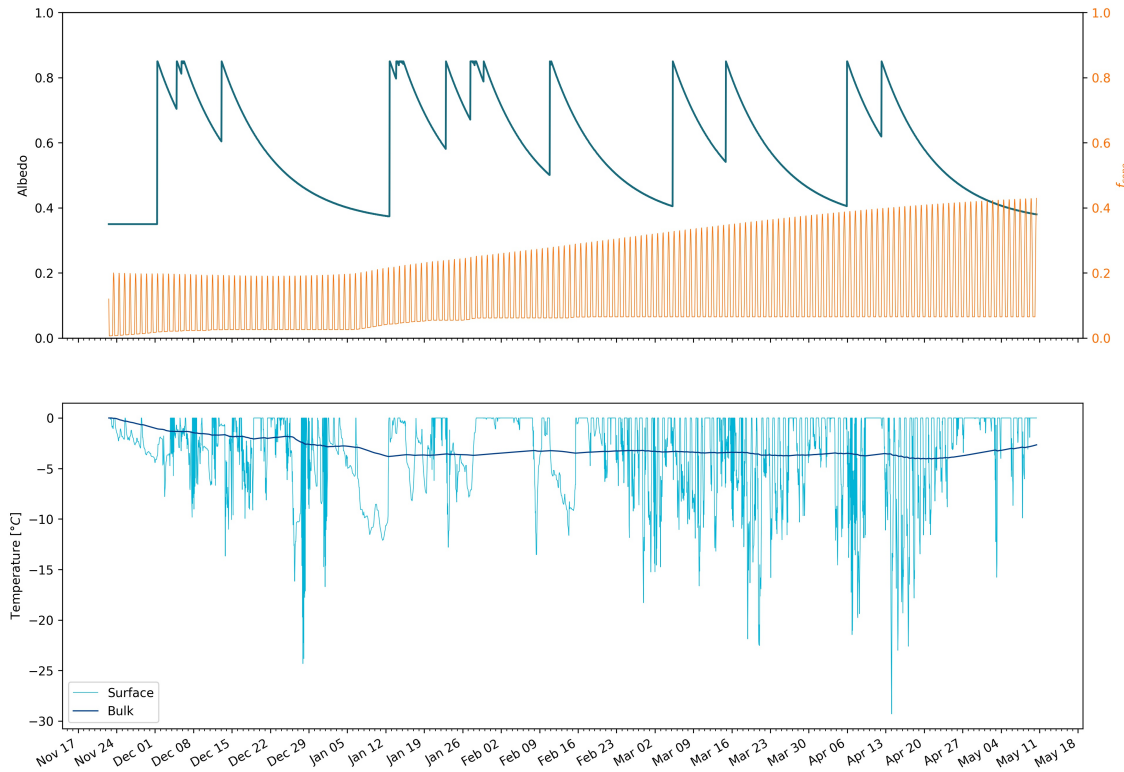


**Figure 7.** Some derived parameters of the model, namely, albedo and  $f_{cone}$  (a), Surface and bulk temperature (b). In (a), the green curve shows how snow and fountain-on events reset albedo between ice albedo and snow albedo. The decay of the snow albedo to ice albedo can also be observed. The orange curve shows how the solar radiation area fraction varied diurnally with variations in the solar elevation angle. In (b), the surface temperature (light blue curve) was forced to be 0 °C during fountain activity. The corresponding bulk temperature is shown with the dark blue curve.

**Table 3.** Summary of mass balance components for the CH21 AIR at the end of the model run on 10<sup>th</sup> May 2021.

Component   CH21		
Input	$M_F$	1,000,041
	$M_{ppt}$	29,533
	$M_{dep}$	4,755
Output	$M_{water}$	196,011
	$M_{ice}$	12,304
	$M_{sub}$	4,747
	$M_{runoff}$	821,267

295 The total water used for the Icestupa development includes contributions from the fountain (96.7%),  
 296 snowfall (2.9 %), deposition (0.5 %) as shown in Table 3. Therefore, in the case of CH21 we used a water  
 297 input of 1,034,328 kg, with a resultant storage efficiency of 19 %.

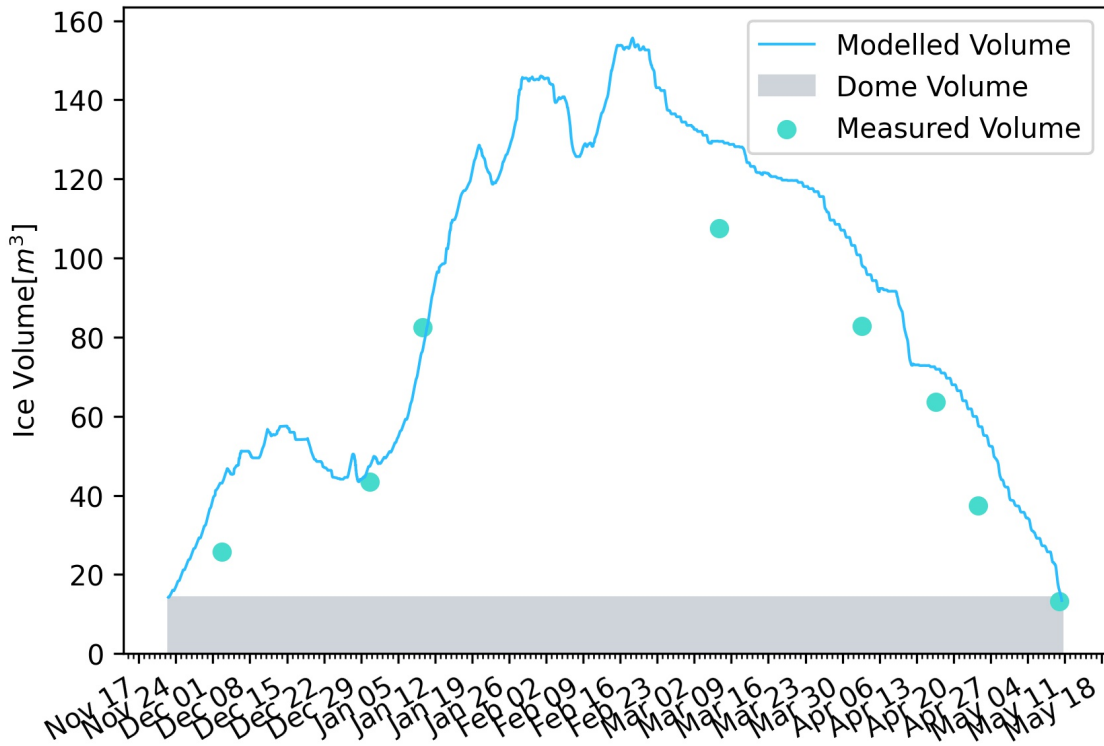


**Figure 8.** Modelled ice volume during the lifetime of the CH21 AIR (blue curve). Green points indicate the validation measurements.

## 5 DISCUSSION

### 298 5.1 Important assumptions

299 In the sensitivity and uncertainty analysis presented above, we did not account for several general  
300 assumptions and parametrisation choices that may cause model errors. Some assumptions and their  
301 potential to cause errors are discussed below.

- 302 • Turbulent Sensible and Latent Heat Fluxes: The method used to calculate the turbulent heat fluxes  
303 by Garratt (1992) assumes that the turbulent heat fluxes are acting over a uniform planar surface to  
304 determine the roughness length. Since our application is on a conical surface, the distance to the ice  
305 surface is not uniform and well defined. Hence,  $z_{ice}$  has no real physical significance here.
- 306 • Droplet flight time loss: Water losses during the flight time of fountain droplets were neglected making  
307 all the fountain spray available for freezing. For the CH21 experiment, inclusion of this parameter does  
308 not influence results since it is already accounted for in the runoff water discharge rate which was at  
309 least  $3 l min^{-1}$ .
- 310 • Nucleation of droplets: Corresponding to droplet flight time, ice/snow formation is also possible before  
311 surface contact if nucleation occurs during flight time. For the CH21 experiment, this process will  
312 further increase the freeze rate and hence the storage efficiency. This process is neglected for model  
313 simplicity.
- 314 • Shape Effects: The suppression of heat exchange between the snow/ice surface and the air adjacent  
315 to the surface effectively slows down snow/ice ablation in spring and promotes the stagnation of the  
316 cold air within topographical depressions (Fujita et al., 2010). The quantitative contribution of the

**Table 4.** AIR Results

AIR	IN21	CH21	CH20	CH19
Max Ice Volume [ $m^3$ ]	703	156	107	1
Storage Efficiency [%]	19	17	14	2
Storage Duration [days]	?	169	93	45

317 atmospheric decoupling over melting snow/ice for the total mass and energy balance is ignored in the  
 318 model.

## 6 CONCLUSIONS

319 We outlined a methodology for estimating ice, liquid water, water vapour and runoff quantities produced  
 320 during the construction of an AIR using measurements of fountain spray rate, air temperature, radiation,  
 321 humidity, pressure, wind and cloudiness at four different study sites. The comparison with all the validation  
 322 measurements at two different dates during the experiment led to satisfying results as shown in Table 4.

323 The model results support the hypothesis that there could be considerable water loss during the formation  
 324 of AIR particularly due to excessive fountain spray. Further experiments at different locations with different  
 325 fountains are required to better understand the influence of construction decisions on the results.

## 7 APPENDIX

### 7.1 Ladakh Icestupa 2014/15

327 A 20 m tall Icestupa (Wangchuk, 2015c) was built in Phyang village, Ladakh at an altitude of 3500  
 328 m a.s.l. Assuming a conical shape with a diameter of 20 m, the corresponding volume of this Icestupa  
 329 becomes 2093  $m^3$  or 1,920  $m^3$  w.e. The fountain sprayed water at a rate of  $210 \text{ l min}^{-1}$  (Wangchuk,  
 330 2015e) from 21<sup>st</sup> January (Wangchuk, 2015a) to at least until 5<sup>th</sup> March 2015 (Wangchuk, 2015b) (around  
 331 43 nights). Assuming fountain spray was active for 8 hours each night, we estimate water consumption to  
 332 be around 4,334  $m^3$ . Thus, during the construction/freezing period of the Icestupa, roughly 56 % of the  
 333 water provided was wasted. The actual water loss is bound to be much higher due to further vapour losses  
 334 during the melting period. This Icestupa completely melted away on 6<sup>th</sup> July 2015 (Wangchuk, 2015d).  
 335 Therefore, the storage duration was 166 days or roughly 5 months.

### 7.2 CH19 AIR

337 The CH19 AIR in the Schwarzsee region lies at 967 m a.s.l.. In the winter (Oct-Apr), mean daily  
 338 maximum and minimum air temperatures vary between -4 and 14 °C. Clear skies are rare, averaging  
 339 around 7 days, and precipitation amounts average 155 mm per month during winter (Meteoblue, 2020).  
 340 The site was situated adjacent to a stream resulting in high humidity values across the study period. Within  
 341 the EP site, an enclosure with a 1.8 m radius was constructed for the experiment. An automatic weather  
 342 station (AWS) was adjacent to the wooden boundary as shown in Fig. 9. The fountain used for spraying  
 343 water had a nozzle diameter of 5 mm and a height of 1.35 m, and was placed in the centre of the wooden  
 344 enclosure. The water was transferred from a spring water source at 1267 m a.s.l. by pipeline and flowed  
 345 via a flowmeter and an air escape valve to the nozzle, where it was sprinkled with a spray radius of around  
 346 1.7 m. The air escape valve was installed to avoid errors in the flow measurements due to air bubbles. In  
 347 addition, a webcam guaranteed a continuous survey of the site during the construction of the Icestupa.

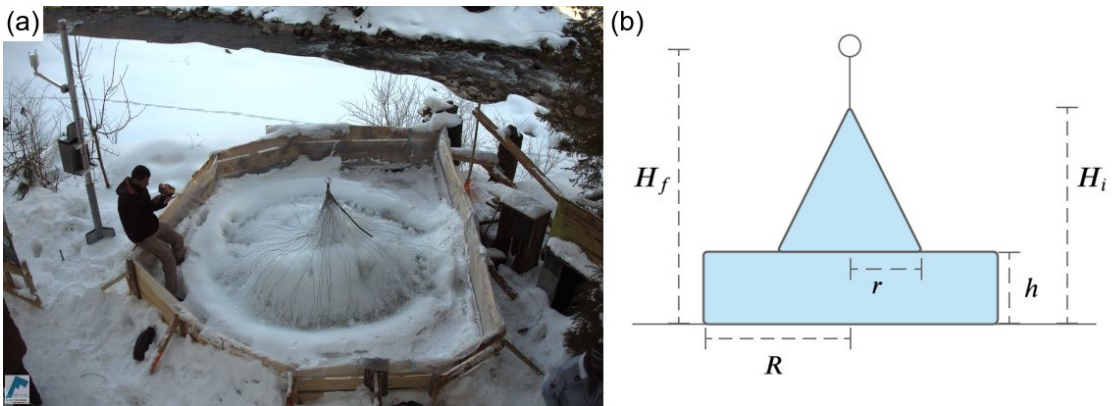


**Figure 9.** (a) The ice structure during the first validation measurement as seen on the webcam image of 14<sup>th</sup> Feb. (b) The corresponding cross section of the EP ice structure with the field estimates of  $r$ ,  $R$ ,  $h$ ,  $H_i$ ,  $H_f$  used to determine the Icestupa volume is shown on the right.

### 348 7.2.1 Weather data corrections

349 Precipitation data was derived from the Plaffeien AWS (IDAWEB, 2019) located 8.8 km away from  
 350 the measurement site at an altitude of 1042 m a.s.l. We recognised during our data analysis that, except  
 351 precipitation, all the other meteorological variables of the EP site correlated much better with the ERA5  
 352 dataset than the nearby Plaffeien AWS dataset. The 2m temperature parameter correlated with air  
 353 temperature ( $r^2 = 0.9$ ), surface pressure parameter correlated with air pressure ( $r^2 = 1$ ) and 10m  
 354 wind speed parameter (derived from horizontal and vertical components) correlated with wind speed  
 355 ( $r^2 = 0.6$ ).

356 Due to a power failure, all data from the EP AWS was lost from 27<sup>th</sup> February 15:20 2019 to 2<sup>nd</sup> March  
 357 15:00 2019 (equivalent to around 7% of the measurement period). During heavy snowfall events, the  
 358 ultrasonic wind sensor was blocked and recorded zero values. ERA5 was used to fill such errors and data  
 359 gaps .

360 The ERA5 grid point chosen (Latitude 46° 38' 24" N, Longitude 7° 14' 24" E) for the EP site was around  
 361 9 km away from the actual site. All the ERA5 variables were therefore fitted with the EP dataset via linear  
 362 regressions. With the modified ERA5 dataset, we were also able to further extend the EP dataset and allow  
 363 the model to run beyond 18<sup>th</sup> March 2019. Precipitation was filled as null values beyond 18<sup>th</sup> March 2019.

### 364 7.2.2 Fountain spray radius of CH19 AIR

365 This fountain spray radius is determined by modelling the projectile motion of the water droplets. Using  
 366 mass conservation, the droplet speed  $v_F$  can be determined from the spray rate  $d_F$  and the diameter  $dia_F$   
 367 of the nozzle as follows:

$$v_F = \frac{d_F}{\pi \cdot dia_F^2 / 4} \quad (30)$$

368 Afterwards, we assume that the water droplets move with an air friction free projectile motion from  
 369 the fountain nozzle with a height  $h_F$  to the ice/ground surface. The resulting spray radius  $r_F$  was then  
 370 determined from the projectile motion equation as follows:

$$r_F = \frac{v_F \cdot \cos\theta_F (v_F \cdot \sin\theta_F + \sqrt{(v_F \cdot \sin\theta_F)^2 + 2 \cdot g \cdot h_F})}{g} \quad (31)$$

371 where  $g = 9.8 \text{ ms}^{-2}$  is the acceleration due to gravity and  $\theta_F = 45^\circ$  is the angle of launch.

### 372 7.2.3 CH19 Field Measurements for validation

373 The volume was determined by decomposing the ice structure into a cylinder (length  $2R$  and height  $h$ )  
 374 and a cone (radius  $r$  and height  $(H_i - h)$ ) through the following equation:

$$V = \pi \cdot R^2 \cdot h + 1/3 \cdot \pi \cdot r^2 \cdot (H_i - h) \quad (32)$$

375 Manual measurements were performed at the end of the freezing period on 14<sup>th</sup> February 16:00 2019  
 376 (only one more fountain run was possible after this date) to estimate  $r, R, h, H_i, H_f$  (see Fig. 9 for the  
 377 different geometry components):

$$0.55 \leq r \leq 1m ; 1.1 \leq R \leq 1.2m ; 0.1 \leq h \leq 0.2m ; 0.6 \leq H_i \leq 0.8m ; 1.3 \leq H_f \leq 1.4m$$

378 The ranges of the variables show the variance of the Icestupa's dimensions across different compass  
 379 orientations. Correspondingly, the volume range estimated for the first validation point was  $0.857 \pm 0.186$   
 380  $\text{m}^3$  on 14<sup>th</sup> February 16:00 2019.

381 The second validation point corresponds to the end of the melting process on 10<sup>th</sup> March 18:00 2019.  
 382 Based on the webcam imagery and manual measurement, a thin layer of ice with an observed thickness  
 383 between 0.01 to 0.06 m could be quantified. This results in the volume range for the second validation to  
 384 be  $0.13 \pm 0.09 \text{ m}^3$  on 11<sup>th</sup> March 2019

385 In reality, the EP ice structure was more cylindrical until a height of 0.2 m and conical afterwards until a  
 386 height of 0.6 m with a radius of 1.18 m. However, we assume a conical shape of this ice structure in order  
 387 to apply the modelling strategy described below.

## REFERENCES

- 388 Apel, H., Abdykerimova, Z., Agalhanova, M., Baimaganbetov, A., Gavrilenko, N., Gerlitz, L., et al. (2018).  
 389 Statistical forecast of seasonal discharge in central asia using observational records: development of a  
 390 generic linear modelling tool for operational water resource management. *Hydrology and Earth System  
 391 Sciences* 22, 2225–2254. doi:10.5194/hess-22-2225-2018
- 392 Bonales, L. J., Rodriguez, A. C., and Sanz, P. D. (2017). Thermal conductivity of ice prepared under  
 393 different conditions. *International Journal of Food Properties* 20, 610–619. doi:10.1080/10942912.  
 394 2017.1306551
- 395 Buck, A. L. (1981). New equations for computing vapor pressure and enhancement factor. *Journal of  
 396 Applied Meteorology and Climatology* 20, 1527 – 1532
- 397 Buytaert, W., Moulds, S., Acosta, L., Bievre, B. D., Olmos, C., Villacis, M., et al. (2017). Glacial melt  
 398 content of water use in the tropical andes. *Environmental Research Letters* 12, 114014. doi:10.1088/  
 399 1748-9326/aa926c
- 400 Chen, Y., Li, W., Deng, H., Fang, G., and Li, Z. (2016). Changes in central asia's water tower: Past, present  
 401 and future. *Nature* doi:10.1088/1748-9326/aa926c
- 402 [Dataset] Copernicus Climate Change Service (C3S) (2017). Era5: Fifth generation of ecmwf atmospheric  
 403 reanalyses of the global climate. [Available at [https://cds.climate.copernicus.eu/  
 404 cdsapp#!/home](https://cds.climate.copernicus.eu/cdsapp#!/home), accessed 2019-10-01]
- 405 Cuffey, K. M. and Paterson, W. S. B. (2010). *The Physics Of Glaciers* (Elsevier)

- 406 Fujita, K. and Ageta, Y. (2000). Effect of summer accumulation on glacier mass balance on the  
407 tibetan plateau revealed by mass-balance model. *Journal of Glaciology* 46, 244–252. doi:10.3189/  
408 172756500781832945
- 409 Fujita, K., Hiyama, K., Iida, H., and Ageta, Y. (2010). Self-regulated fluctuations in the ablation of a snow  
410 patch over four decades. *Water Resources Research* 46, W11541. doi:10.1029/2009WR008383
- 411 Garratt, J. R. (1992). *The Atmospheric Boundary Layer* (Cambridge University Press)
- 412 Grossman, D. (2015). As himalayan glaciers melt, two towns face the fallout [Available at  
413 [https://e360.yale.edu/features/as\\_himalayan\\_glaciers\\_melt\\_two\\_towns\\_](https://e360.yale.edu/features/as_himalayan_glaciers_melt_two_towns_face_the_fallout)  
414 [face\\_the\\_fallout](https://e360.yale.edu/features/as_himalayan_glaciers_melt_two_towns_face_the_fallout), accessed 2019-10-01]
- 415 Hock, R. (2005). Glacier melt: a review of processes and their modelling. *Progress in Physical Geography:  
416 Earth and Environment* 29, 362–391
- 417 Hock, R., Rasul, G., Adler, C., Cáceres, B., Gruber, S., Hirabayashi, Y., et al. (2019). 2019: High mountain  
418 areas. *IPCC Special Report on the Ocean and Cryosphere in a Changing Climate* [H.-O. Pörtner, D.C.  
419 Roberts, V. Masson-Delmotte, P. Zhai, M. Tignor, E. Poloczanska, K. Mintenbeck, A. Alegría, M. Nicolai,  
420 A. Okem, J. Petzold, B. Rama, N.M. Weyer (eds.)]
- 421 Hoelzle, M., Barandun, M., Bolch, T., Fiddes, J., Gafurov, A., Muccione, V., et al. (2019). *The status and  
422 role of the alpine cryosphere in Central Asia*. doi:10.4324/9780429436475-8
- 423 Hori, M., Aoki, T., Tanikawa, T., Motoyoshi, H., Hachikubo, A., Sugiura, K., et al. (2006). In-situ  
424 measured spectral directional emissivity of snow and ice in the 8–14 micrometer atmospheric window.  
425 *Remote Sensing of Environment* 100, 486 – 502
- 426 [Dataset] IDAWEB (2019). Meteoswiss, federal office of meteorology and climatology. [Available at  
427 <https://gate.meteoswiss.ch/idaweb/login.do>, accessed 2019-10-01]
- 428 Immerzeel, W. W., Lutz, A. F., Andrade, M., Bahl, A., Biemans, H., Bolch, T., et al. (2019). Importance  
429 and vulnerability of the world's water towers. *Nature* 577, 364 – 369. doi:10.1038/s41586-019-1822-y
- 430 Meteoblue (2020). Climate schwarzsee [Available at [https://www.meteoblue.com/en/weather/historyclimate/climatemodelled/schwarzsee\\_switzerland\\_11790334](https://www.meteoblue.com/en/weather/historyclimate/climatemodelled/schwarzsee_switzerland_11790334), accessed 2019-10-01]
- 431 Mölg, T. and Hardy, D. R. (2004). Ablation and associated energy balance of a horizontal glacier surface  
432 on kilimanjaro. *J. Geophys. Res.-Atmos.* 109, 1–13. doi:10.1029/2003JD004338
- 433 Nüsser, M., Dame, J., Kraus, B., Baghel, R., and Schmidt, S. (2019a). Socio-hydrology of artificial glaciers  
434 in ladakh, india: assessing adaptive strategies in a changing cryosphere. *Regional Environmental Change*  
435 doi:10.1007/s10113-018-1372-0
- 436 Nüsser, M., Dame, J., Parveen, S., Kraus, B., Baghel, R., and Schmidt, S. (2019b). Cryosphere-Fed  
437 Irrigation Networks in the Northwestern Himalaya: Precarious Livelihoods and Adaptation Strategies  
438 Under the Impact of Climate Change. *Mountain Research and Development* 39. doi:10.1659/  
439 MRD-JOURNAL-D-18-00072.1
- 440 Oerlemans, J. and Knap, W. H. (1998). A 1 year record of global radiation and albedo in the  
441 ablation zone of morteratschgletscher, switzerland. *Journal of Glaciology* 44, 231–238. doi:10.  
442 3189/S0022143000002574
- 443 Scherrer, S. C. (2020). Temperature monitoring in mountain regions using reanalyses: lessons from the  
444 alps. *Environmental Research Letters* 15, 044005
- 445 Schmidt, L. S., Aðalgeirsdóttir, G., Guðmundsson, S., Langen, P. L., Pálsson, F., Mottram, R., et al. (2017).  
446 The importance of accurate glacier albedo for estimates of surface mass balance on vatnajökull: evaluating  
447 the surface energy budget in a regional climate model with automatic weather station observations. *The  
448 Cryosphere* 11, 1665–1684. doi:10.5194/tc-11-1665-2017

- 451 Tetens, O. (1930). Über einige meteorologische begriffe. z. *Geophys.* 6, 297–309
- 452 Unger-Shayesteh, K., Vorogushyn, S., Farinotti, D., Gafurov, A., Duethmann, D., Mandychev, A., et al.  
453 (2013). What do we know about past changes in the water cycle of central asian headwaters? a review.  
454 *Global and Planetary Change* 110, 4 – 25. doi:10.1016/j.gloplacha.2013.02.004. Water in Central Asia  
455 – Perspectives under global change
- 456 Wangchuk, S. (2014). Ice stupa artificial glaciers of ladakh [Available at [www.indiegogo.com/projects/ice-stupa-artificial-glaciers-of-ladakh#/](http://www.indiegogo.com/projects/ice-stupa-artificial-glaciers-of-ladakh#/), accessed 2019-10-01]
- 457 Wangchuk, S. (2015a). The good news at ice stupa 24th january 2015 [Available at <http://icestupa.org/news/the-good-news-at-ice-stupa>, accessed 2019-10-01]
- 458 Wangchuk, S. (2015b). Ice stupa artificial glacier inaugurated  
459 5th of march 2015 [Available at <http://icestupa.org/news/ice-stupa-artificial-glacier-inaugurated-5th-of-march>, accessed  
460 2019-10-01]
- 461 Wangchuk, S. (2015c). Ice stupa surpasses guiness world record [Available at <http://icestupa.org/news/ice-stupa-surpasses-guinness-world-record>, accessed 2019-10-01]
- 462 Wangchuk, S. (2015d). Ice stupa way of celebrating a special day [Available at <http://icestupa.org/news/ice-stupa-way-of-celebrating-a-special-day6th-of-ju>, accessed  
463 2019-10-01]
- 464 Wangchuk, S. (2015e). World water day at ice stupa [Available at <http://icestupa.org/news/world-water-day-at-ice-stupa>, accessed 2019-10-01]
- 465 WMO (2018). *Guide to Instruments and Methods of Observation* (World Meteorological Organization ;  
466 2018 (2018 Edition))
- 467 Woolf, H. M. (1968). *On the Computation of Solar Elevation Angles and the determination of sunrise and*  
468 *sunset times* (National Aeronautics and Space Administration)
- 469 Zhou, S., Kang, S., Gao, T., and Zhang, G. (2010). Response of zhadang glacier runoff in nam co basin,  
470 tibet, to changes in air temperature and precipitation form. *Chinese Science Bulletin* 55, 2103–2110.  
471 doi:10.1007/s11434-010-3290-5